

Experimental validation of a complex, large-scale, rigid-body mechanism

Cite as:

M. Langerholc, M. Česnik, J. Slavič and M. Boltežar: Experimental validation of a complex, large-scale, rigid-body mechanism. Engineering Structures, Vol. 36 (2012), Pages 220-227. DOI: 10.1016/j.engstruct.2011.12.014

Marko Langerholc^{a,b}, Martin Česnik^a, Janko Slavič^{a,*}, Miha Boltežar^a

^aUniversity of Ljubljana, Faculty of Mechanical Engineering, Aškerčeva 6, 1000 Ljubljana, SI, Slovenia

^bKnauf Insulation d.o.o., Trata 32, 4250 Škofja Loka, SI, Slovenia

Abstract

This study presents an approach to an experimental validation of a complex, large-scale, multi-body mechanism model with diverse body inertia and geometry properties, exposed to an arbitrary kinematic excitation. Such an approach was used to analyze and predict the dynamical behaviour of a complex, 24-DOF, pendulum system with a relatively large dimensions. To obtain the theoretical dynamical response a computational dynamics approach was used in order to establish a constraint-based, simplified, planar, rigid-body numerical model. To validate the model, a special experimental approach was employed that overcame the difficulties related to the analyzed system's size, many rotating components and simultaneous measuring requirements. Consequently, a combination of conventional and wireless signal-streaming measuring setups, which transmitted the signal through the purposely set-up wireless network, were employed. The model is validated by comparing the simulated and experimentally obtained kinematical and dynamical quantities to justify rigidity of the model's components and the simplified planar modelling. The validated model's ability to predict hard-to-measure system's response is demonstrated.

Keywords: computational dynamics, vibrations, concurrent experiments, wireless measurements

1. Introduction

The dynamical behaviour of large-scale, complex, multi-body systems has been the subject of extensive research for many years. However, whichever approach to such an analysis is employed, i.e. theoretical or experimental [1], limitations always exist because of the analyzed system's size, shape or various nonlinearities that make a reliable dynamical behaviour estimation difficult.

*Corresponding author. Tel.: +386 1 4771 226 (direct line);
fax: +386 1 2518 567

By employing a theoretical approach to determine a complex dynamical system's response we may choose from different approaches, among which the classical Newtonian or Lagrangian formulations are popular [2]-[5]. When analyzing a large-scale, multi-body, dynamical system with bodies that possess diverse inertia, stiffness and damping properties [6]-[8], the classical acquisition of motion equations becomes cumbersome due to the complex system's energy definition. Therefore, the classical techniques have been reformulated and adjusted for computer implementation [9]-[11]. A so-called *computational dynamics* approach has been widely accepted and used for a determination of the dynamical response of different complex machines and structures, that are exposed to an arbitrary loading [12]-[15].

When we choose to analyze a dynamical system experimentally, other difficulties must be overcome. If concurrent measurements are necessary the wireless measuring approach is one of the means to analyze a relatively large system [16, 17]. If the measuring signal needs to be acquired over a relatively large distance, then field measurements need to be considered [18]. In any case, a numerical model validated by experimental measurements gives us an edge when predicting the system's dynamical response to arbitrary excitations.

In this paper, we present an experimental procedure to validate the numerical model of a complex multi-body system. The procedure is utilized on the pendulum system [19], one of the most important segments of the technical insulation production process [20], (Fig. 1). The main function of the pendulum system is to provide a homogeneous, multi-layer distribution of uncrimped stone wool by rapidly folding the continuous material (Fig. 2). The dynamical issues that occur during the pendulum system's operation are directly related to the folding-process velocity, which causes machine-strength problems and undesired vibrations for the whole structure. In reality, there are many operating conditions related to the pendulum system that dictate different pendulum excitations and kinematic conditions, which are of vital importance for the product's quality and the mechanism's strength. For this reason, the presented research describes a feasible approach to the experimental validation of the numerical model, which is later used to study the hard-to-measure dynamics.

The pendulum system is analyzed as a kinematically driven, rigid-body mechanism. To simplify the numerical analysis the mechanism was presumed to be symmetric and a planar computational dynamics approach was used to obtain the numerical model. To validate the model several experiments were conducted on the existing pendulum system during the real-time production process. The measurements of accelerations, transverse and longitudinal deformations were made to obtain the whole dynamical response. Due to the pendulum system's size, its rotating components and their vast motion envelope, the experimental setup presented difficult conditions for making the measurements. Therefore, an approach of mixed measurements, i.e., conventional and wireless, was employed to capture the concurrent relations between the measured quantities. The model validation was executed by comparing the theoretical and the experimentally obtained results.

The paper is organized as follows: In section 2, the theoretical background of the computational dynamics approach is explained, followed by the numerical model of the pendulum system in section 3. In section 4, the experiments and the model validation are explained in detail. Finally, a short discussion and the conclusions are given in sections 5 and 6.

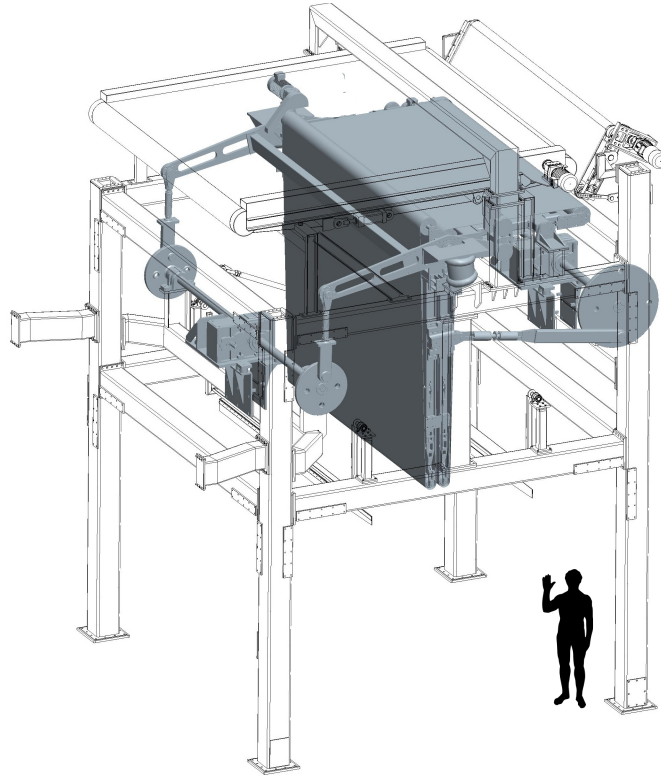


Figure 1: Pendulum system structure: Pendulum - shaded, Framework - wireframe

2. Theoretical background

The analyzed system is defined as planar, kinematically driven, rigid-body mechanism with zero dynamical DOF. Since we are dealing with a full inverse dynamics problem, the implementation of the dynamic equations of motion is not necessary to determine the system's coordinates, velocities and accelerations. However, for the numerical model validation, also the estimation of the torques and specific constraint forces is needed. These can only be determined, if the system's inertia properties, i.e., dynamic equations of motion, are also implemented in the model. The constraint forces and the torques are then determined using the technique of Lagrange multipliers.

In the following, the establishment of the constraint equations is explained first, followed by the determination of the system's positions, velocities and acceleration. For the constraint forces and torques determination, the implementation of the equations of motion in the full inverse dynamics problem is shown. Only a brief explanation of the theoretical approach is given here; for an extensive explanation, see [9].

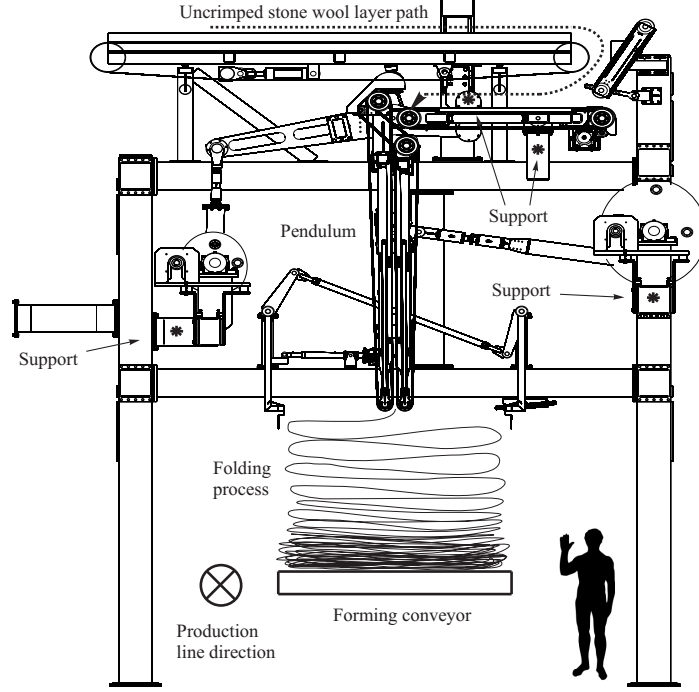


Figure 2: Pendulum system folding function

2.1. Constraint equations

Let us consider two rigid bodies i and j , connected at the point P (Fig. 3). The equation of a *revolute joint* is [9]

$$\mathbf{R}^i + \mathbf{T}^i \bar{\mathbf{v}}_P^i - \mathbf{R}^j - \mathbf{T}^j \bar{\mathbf{v}}_P^j = \mathbf{0}, \quad (1)$$

where \mathbf{R}^i is the position of the local coordinate systems, $\bar{\mathbf{v}}_P^i = \{\bar{x}_P^i, \bar{y}_P^i\}^T$ is the i -th body's local position vector of point P and \mathbf{T}^i is the i -th body transformation matrix:

$$\mathbf{T}^i = \begin{bmatrix} \cos \theta^i & -\sin \theta^i \\ \sin \theta^i & \cos \theta^i \end{bmatrix}, \quad (2)$$

where θ^i is the angle of the i -th body's local coordinate system with respect to the global coordinate system.

For the special cases, when the i -th body's translations are fixed at the point P or the position is prescribed, eq. (1) becomes

$$\mathbf{R}^i + \mathbf{T}^i \bar{\mathbf{v}}_P^i - \mathbf{c}_P^i = \mathbf{0}, \quad (3)$$

$$\mathbf{R}^i + \mathbf{T}^i \bar{\mathbf{v}}_P^i - \mathbf{h}^i(t) = \mathbf{0} \quad (4)$$

respectively, where $\mathbf{c}_P^i = \{c_{P1}^i, c_{P2}^i\}^T$ is a constant position vector of the fixed pin, and $\mathbf{h}^i(t) = \{h_1^i(t), h_2^i(t)\}^T$ are the arbitrary, time-dependent, kinematic excitations.

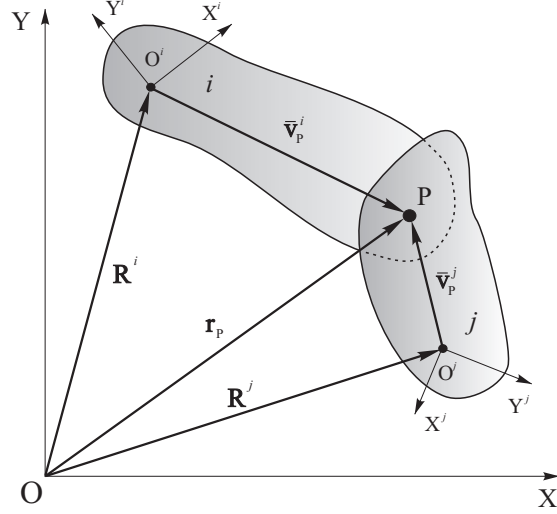


Figure 3: Revolute joint between two rigid bodies

2.2. Kinematics

For a computer implementation all the system coordinates are written in the form [9]

$$\mathbf{e} = [\mathbf{e}_1, \mathbf{e}_2, \dots, \mathbf{e}_{n_b}]^T, \quad (5)$$

where n_b is the number of bodies and

$$\mathbf{e}^i = [R_x^i, R_y^i, \theta^i]^T \quad (6)$$

are the *absolute coordinates* of the i -th body. R_x^i and R_y^i are the components of the global position vector of the i -th body, usually its center of gravity. A *constraint vector* is defined [9]:

$$\mathbf{C}(\mathbf{e}, t) = [C_1(\mathbf{e}, t), C_2(\mathbf{e}, t), \dots, C_n(\mathbf{e}, t)]^T = \mathbf{0}, \quad (7)$$

where $C_k(\mathbf{e}, t)$ are the scalar constraint equations (1-4) of the whole system. The constraint vector (7) represents a set of nonlinear algebraic equations, which are solved by employing the *Newton-Raphson* algorithm [9], to obtain the system configuration.

The system velocities and accelerations are obtained by differentiating the constraint vector (7) with respect to time:

$$\mathbf{C}_e \dot{\mathbf{e}} + \mathbf{C}_t = \mathbf{0}, \quad (8)$$

$$\mathbf{C}_e \ddot{\mathbf{e}} - \mathbf{Q}_d = \mathbf{0}, \quad (9)$$

where $(\cdot) = \partial/\partial t$, and

$$\begin{aligned} \mathbf{C}_t &= \frac{\partial \mathbf{C}(\mathbf{e}, t)}{\partial t}, \\ \mathbf{C}_e &= \frac{\partial \mathbf{C}(\mathbf{e}, t)}{\partial \mathbf{e}}, \\ \mathbf{Q}_d &= -(\mathbf{C}_e \dot{\mathbf{e}})_e - 2 \mathbf{C}_{et} \dot{\mathbf{e}} - \mathbf{C}_{tt}. \end{aligned}$$

From (8) and (9) the vectors of the absolute system velocities $\dot{\mathbf{e}}$ and accelerations $\ddot{\mathbf{e}}$ are calculated for each simulation step using the accepted system-configuration vector (5) from the Newton-Raphson algorithm. By obtaining the full kinematic descriptions of the system bodies $(\mathbf{e}, \dot{\mathbf{e}}, \ddot{\mathbf{e}})$, the position \mathbf{r}_P^i , velocity $\dot{\mathbf{r}}_P^i$ and acceleration $\ddot{\mathbf{r}}_P^i$ of an arbitrary P on the i -th body can be determined from (5) and (6) as

$$\mathbf{r}_P^i = \mathbf{R}^i + \mathbf{T}^i \bar{\mathbf{v}}_P^i, \quad (10)$$

$$\dot{\mathbf{r}}_P^i = \dot{\mathbf{R}}^i + \dot{\theta}^i \frac{\partial \mathbf{T}^i}{\partial \theta^i} \bar{\mathbf{v}}_P^i, \quad (11)$$

$$\ddot{\mathbf{r}}_P^i = \ddot{\mathbf{R}}^i - (\dot{\theta}^i)^2 \mathbf{T}^i \bar{\mathbf{v}}_P^i + \ddot{\theta}^i \frac{\partial \mathbf{T}^i}{\partial \theta^i} \bar{\mathbf{v}}_P^i. \quad (12)$$

2.3. Equations of motion and constraint forces

The equations of motion are obtained by employing the virtual work principle together with the d'Alembert principle [10]

$$\mathbf{M} \ddot{\mathbf{e}} = \mathbf{Q}_e + \mathbf{Q}_c, \quad (13)$$

where $\ddot{\mathbf{e}}$ is the vector of system absolute accelerations, and

$$\mathbf{Q}_e = \left[\mathbf{Q}_e^{1T} \quad \mathbf{Q}_e^{2T} \quad \dots \quad \mathbf{Q}_e^{iT} \quad \dots \quad \mathbf{Q}_e^{n_b T} \right]^T, \quad (14)$$

$$\mathbf{Q}_c = \left[\mathbf{Q}_c^{1T} \quad \mathbf{Q}_c^{2T} \quad \dots \quad \mathbf{Q}_c^{iT} \quad \dots \quad \mathbf{Q}_c^{n_b T} \right]^T, \quad (15)$$

$$\mathbf{M} = \begin{bmatrix} \mathbf{M}^1 & & & & & \\ & \mathbf{M}^2 & & & & \\ & & \ddots & & & \\ & & & \mathbf{M}^i & & \\ & 0 & & & \ddots & \\ & & & & & \mathbf{M}^{n_b} \end{bmatrix}, \quad (16)$$

where \mathbf{Q}_c^i and \mathbf{Q}_e^i are the i -th body's generalized constraint and external forces, respectively. In the case when the origins of the bodies' local coordinate systems coincide with the bodies' centers of gravity, the mass matrix \mathbf{M}^i is [9]

$$\mathbf{M}^i = \begin{bmatrix} m^i \mathbf{I} & \mathbf{0} \\ \mathbf{0} & J^i \end{bmatrix}, \quad (17)$$

where m^i and J^i are the i -th body's mass and mass moment of inertia, respectively.

The joints forces are obtained by expressing the generalized constraint forces with the constraint Jacobian matrix [9]

$$\mathbf{Q}_c = -\mathbf{C}_e^T \boldsymbol{\lambda}, \quad (18)$$

where $\boldsymbol{\lambda}$ is a vector of *Lagrange multipliers*. For the pendulum model, the generalized forces of the i -th body's k -th joint are determined as

$$\left(\mathbf{Q}_c\right)_k = -\left(\mathbf{C}_k\right)_{e^i}^T \boldsymbol{\lambda}_k = \left[F_{x_k}^i \ F_{y_k}^i \ M_{x_k}^i\right]^T, \quad (19)$$

where $\boldsymbol{\lambda}_k$ is the vector of Lagrange multipliers, $F_{x_k}^i, F_{y_k}^i$ are the horizontal and vertical component of the force, and $M_{x_k}^i$ generalized moment at the k -th joint.

3. Numerical model

The pendulum-mechanism numerical model in its reference position is shown in Fig. 4. The model consists of 8 bodies, labeled with the capital letters A-H. The bodies are constrained either with revolute joints (1) or fixed pins (3) at the points (P_1, \dots, P_{12}). The body A, labeled also as "Pendulum", is driven through the body B with the main drive F. Additionally, the lifting drive H is included.

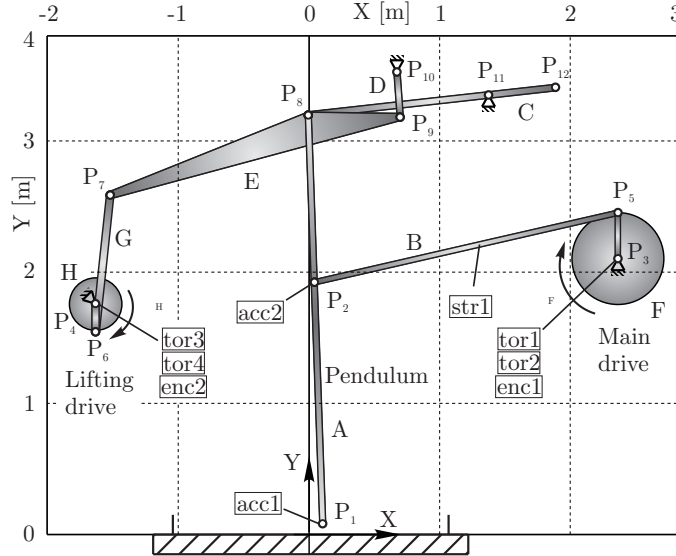


Figure 4: Pendulum model in the reference position, measuring locations for validation (squared)

The total number of DOF is 24. To make the pendulum model kinematically driven, all the DOF are specified; 22 constraints and 2 kinematic excitations. The system's absolute coordinates vector (6) and constraint vector (7) are defined as

$$\mathbf{e} = \left[R_x^A, R_y^A, \theta^A, R_x^B, R_y^B, \theta^B, \dots, R_x^H, R_y^H, \theta^H, \right]^T, \quad (20)$$

$$\mathbf{C}(\mathbf{e}, t) = \left[\text{Rev}(A, B), \text{Rev}(A, E), \text{Rev}(A, C), \text{Rev}(E, D), \text{Rev}(E, G), \right. \\ \left. \text{Rev}(G, H), \text{Rev}(B, F), \text{Fix}(F), \text{Fix}(D), \text{Fix}(C), \text{Fix}(H), \theta^F(t), \theta^H(t) \right]^T, \quad (21)$$

where $\text{Rev}(\cdot, \cdot)$ and $\text{Fix}(\cdot)$ stand for the revolute joint between two bodies and the fixed pin of a body, respectively. $\theta^F(t)$ and $\theta^H(t)$ are specifically defined kinematic excitations of the pendulum drives. For the sake of brevity, only two constraints are stated explicitly:

$$\begin{aligned} \text{Rev}(A, E) &= \mathbf{R}^A + \mathbf{T}^A \bar{\mathbf{v}}_{P_8}^A - \mathbf{R}^E - \mathbf{T}^E \bar{\mathbf{v}}_{P_8}^E = \mathbf{0}, \\ \text{Fix}(C) &= \mathbf{R}^C + \mathbf{T}^C \bar{\mathbf{v}}_{P_{11}}^C - \mathbf{c}_{P_{11}}^C = \mathbf{0}, \end{aligned}$$

where \mathbf{R}^k is the absolute position vector of the body's center of gravity, $\bar{\mathbf{v}}_j^k$ is the position of the connection point P_j in the body's local coordinate system, and \mathbf{c}_j^k is the position vector of the fixed point P_j , Fig. 5.

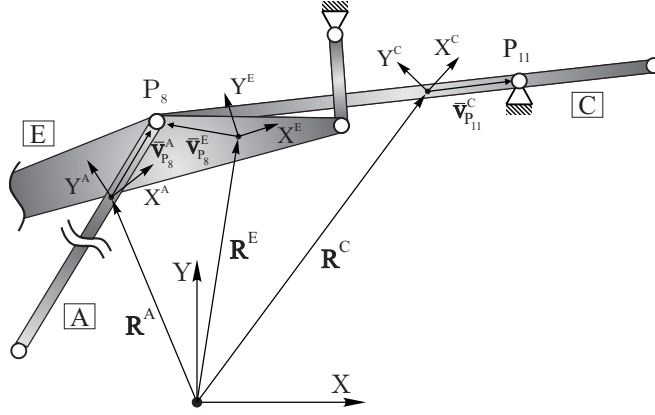


Figure 5: Pendulum model detail; establishment of the constraint equations

The mass matrix \mathbf{M} is defined as (16):

$$\mathbf{M} = \begin{bmatrix} \mathbf{M}^1 & & 0 \\ & \ddots & \\ 0 & & \mathbf{M}^8 \end{bmatrix}$$

with the i -th body's mass matrix \mathbf{M}^i as (17). The vector of external forces (15) consists of the system's gravity forces:

$$\mathbf{Q}_e = \left[-m^1 g, \dots, -m^8 g \right]^T,$$

where g is a gravitational constant.

3.1. Quantities for model validation

For the model validation, different accelerations, strains and torques need to be estimated. At the measured locations (Fig. 4), these quantities are obtained from the model with eq. (12) and (19) as follows:

1. Accelerations “acc1” and “acc2”:

$$\text{acc1} : \ddot{\mathbf{r}}_{P_1}^A = \ddot{\mathbf{R}}^A - (\dot{\theta}^A)^2 \mathbf{T}^A \bar{\mathbf{v}}_{P_1}^A + \ddot{\theta}^A \frac{\partial \mathbf{T}^A}{\partial \theta^A} \bar{\mathbf{v}}_{P_1}^A, \quad (22)$$

$$\text{acc2} : \ddot{\mathbf{r}}_{P_2}^B = \ddot{\mathbf{R}}^B - (\dot{\theta}^B)^2 \mathbf{T}^B \bar{\mathbf{v}}_{P_2}^B + \ddot{\theta}^B \frac{\partial \mathbf{T}^B}{\partial \theta^B} \bar{\mathbf{v}}_{P_2}^B, \quad (23)$$

2. Normal strain “str1”:

$$\text{str1} : \sigma_x = -A^{-1} \lambda_{P_5}^x, \quad (24)$$

where σ_x denotes the axial stress only due to the horizontal joint force component, $\lambda_{P_5}^x$ is the Lagrange multiplier, associated with this horizontal force and A is the pendulum’s arm cross-section.

3. Torque “tor1” - “tor4”:

$$\text{tor1, tor2} : M_{P_3} = -\lambda_{P_3}^\phi, \quad (25)$$

$$\text{tor3, tor4} : M_{P_4} = -\lambda_{P_4}^\phi. \quad (26)$$

where $\lambda_{P_k}^\phi$ are the Lagrange multipliers, related to the prescribed kinematic excitations.

4. Experimental validation

The experiments on the pendulum system were designed to validate the numerical model from the kinematical and dynamical points of view. Mixed quantities measurements, i.e., accelerations, strains and shaft angles, were therefore executed for the purposely chosen locations on the pendulum mechanism.

4.1. Experimental setups

In order to obtain the entire dynamical response and the exact interacting relations of the measured quantities, the measurements needed to run simultaneously, which meant that the size of the pendulum presented a problem. This problem was resolved by employing wireless simultaneous signal streaming NI WLS-9163 modules, which were required to be firmly fixed on the moving components. For these modules, an uninterruptible power supply was ensured from the attached 12V 2.9Ah lead-acid batteries (Fig. 8).

Another advantage of using the wireless signal streaming modules was the ability to conduct measurements on the rotating parts, which is otherwise difficult to do. The wireless modules transmitted the signal simultaneously through a purposely set-up wireless network. Where possible, the measurements were also executed with conventional equipment, i.e., NI cDAQ-9172 acquisition modules with the appropriate analog input modules and an external power source. The measured quantities and measuring locations on the pendulum system are shown in Fig. 6, marked with asterisks. There are 12 measuring locations: 3 for acceleration (acc1-acc3), 4 for transverse strain (tor1-tor4), 2 for normal strain (str1, str2) and 2 for shaft angle (enc1, enc2) measurements. The labels supp1-suppl4 mark the pendulum supports on the framework structure.

The piezoelectric charge accelerometers PCB-357B40 with conditioning amplifier, analog input modules and a combination of the wireless and standard data-acquisition modules, were used for measuring the accelerations acc1-acc3. An example of two experimental setups is shown in Fig. 7. For the transverse strains tor1-tor4 measurements,

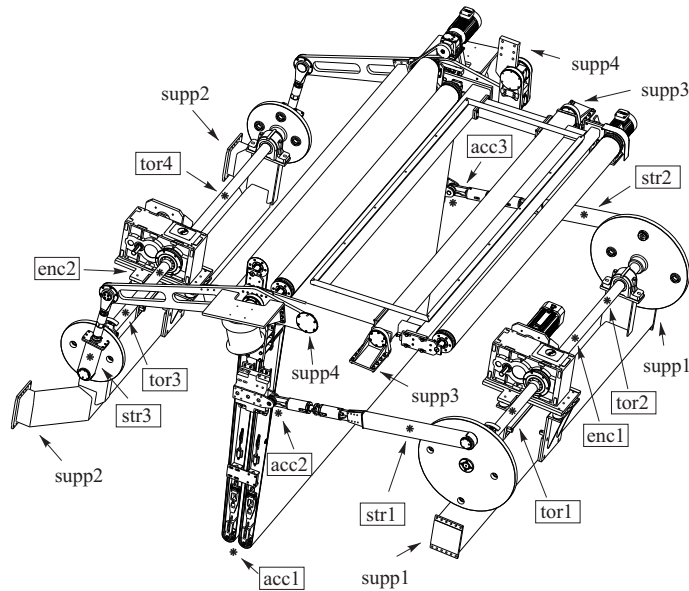


Figure 6: Measured quantities and measuring locations (squared): acceleration (acc1-acc3), normal strain (str1, str2), transverse strain (tor1-tor4) and shaft angle (enc1, enc2)

type HBM-1-XY21-6/120 strain gages were used with the wireless measuring signal acquisition equipment, Fig. 8. The normal strains str1-str3 were measured with type HBM-1-LY11-6/120A strain gages with a combination of the wireless and conventional measuring equipment. The experimental setup is shown in Fig. 9.

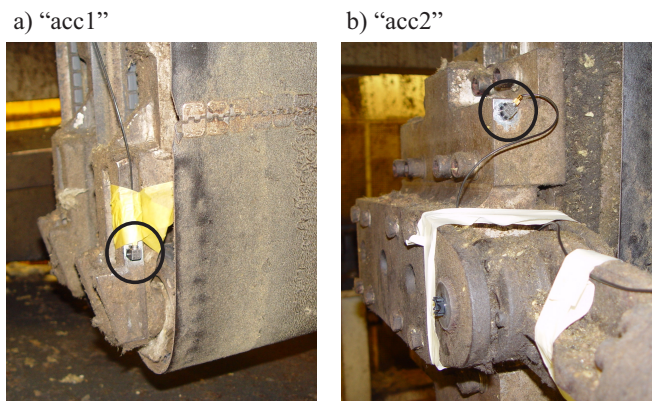


Figure 7: Acceleration measurements setups (circled)

The pendulum mechanism's position was measured with respect to the rotation of the main pendulum shafts. The reference position (Fig. 4) was chosen and marked with digital encoders (Fig. 10). The optical sensors Pepperl+Fuchs,

a) “tor2”

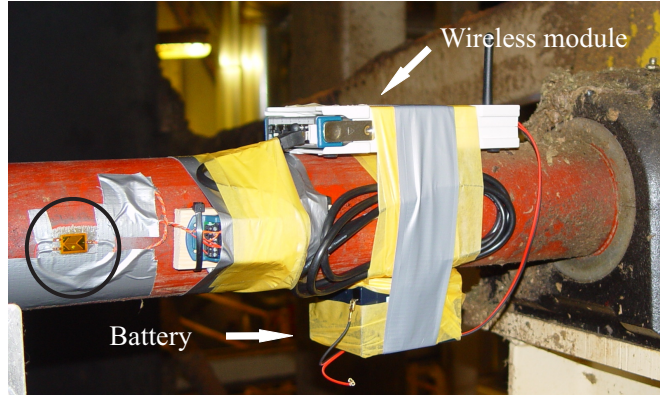


Figure 8: The transverse strain measurement location (circled), wireless signal streaming module and battery

a) “str1”

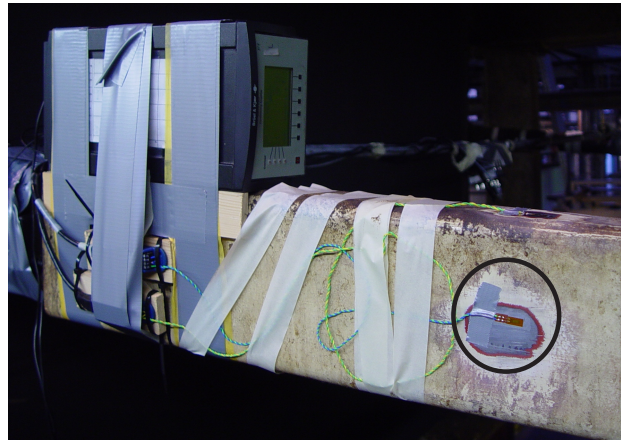


Figure 9: The normal strain measurement location (circled)

type GLV12-8-200, were used to identify the reference position during the pendulum’s movement.

All the measurements were executed with a 20 s duration for several different operating velocities and kinematic excitations $\theta^F(t)$ and $\theta^H(t)$. The sampling frequency for the normal strain and acceleration measurements was 5 kHz and for the transverse strains measurements it was 1.6 kHz.

4.2. Model validation

The pendulum model’s validation was performed through the comparison of the numerical results and experimentally obtained measurements for the same pendulum excitations. The model is validated when the comparison of

a) “enc2”



Figure 10: The digital encoder and the optical sensors' setup for the pendulum shaft-angle measurement

the kinematical and dynamical results are in agreement, and the planar rigid-body approach to numerical modelling proves justified.

From the extensive experimental data obtained, all the measured quantities were found to be periodic. Therefore, the independent variable for the results' comparison was chosen to be the shaft angle ϕ_F with respect to the pendulum's reference position (Fig. 4), which was obtained from the encoder (Fig. 10).

To determine the significance of the pendulum's deformability, the accelerations $acc1$ and $acc2$ (Fig. 6) are compared in Fig. 11, where the measured and simulated horizontal accelerations of the points P_1 and P_2 (22, 23) are shown. Similar trends are evident and it is clear that for a global kinematic description the model may consist of rigid bodies.

For the purpose of justifying the planar modelling, a comparison between the simulated and experimentally obtained torques and stresses with respect to the pendulum mechanism's symmetry is analyzed.

First, the comparison between the simulated torques (25, 26) and the torques calculated from the measured transverse strains ($tor1$ - $tor4$) and the shafts' geometry and material properties is presented in Fig. 12 and Fig. 13.

A discrepancy can be seen in the experimentally obtained torques $tor1$ - $tor2$ and $tor3$ - $tor4$. We could attribute this difference to the machine's manufacturing and assembly defects and the experimental setups' imperfections. In any case, the numerical model manages to capture both real torques' trends well with respect to the pendulum's mechanism complexity.

Second, the comparison between the simulated and experimentally obtained axial stress for body B (Fig. 4) is made (Fig. 14). The simulated stress is obtained from the forces, calculated from eq. (24), for points P_2 and P_5 , and the experimental stresses are calculated from the normal strains (Fig. 6). The difference between the simulated and experimental stresses originates from other effects that influence the deformations of body B (Fig. 4), i.e., buckling and bending. These deformation modes could not be captured due to the rigid-body modelling. However, the absolute

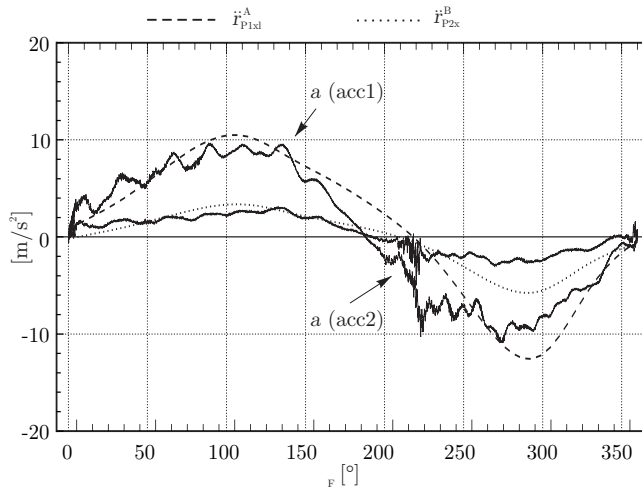


Figure 11: Comparison between theoretically and experimentally obtained horizontal accelerations on the pendulum

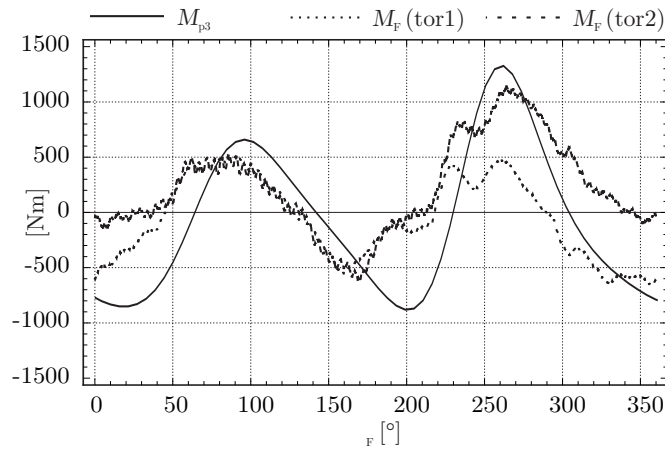


Figure 12: Comparison between the simulated and experimentally obtained torques for the main pendulum drive

stress amplitudes remain similar and the stress is periodic.

The results shown in this section represent the most relevant fraction of the extensive amount of experimental and simulated data obtained for many different pendulum-system operating conditions. From this data the planar pendulum modelling proved to be justified. It is concluded that the planar pendulum model describes both the kinematics and dynamics globally accurately and is therefore considered as validated.

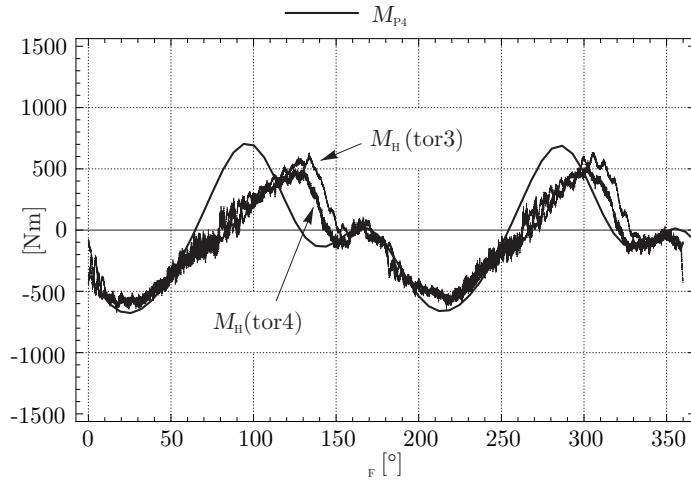


Figure 13: Comparison between the simulated torque and the experimentally obtained torques for the lifting pendulum drive

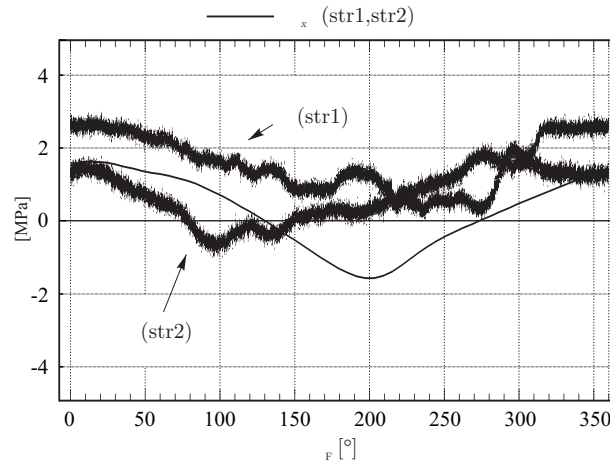


Figure 14: Comparison between the theoretically and experimentally obtained normal stress in the pendulum arm

5. Discussion

The validated numerical model can be used to predict the kinematical and dynamical response to arbitrary kinematic excitations. These predictions can reliably be made at the locations on the pendulum's structure where the measurements are difficult to execute. Some important results for the performance of the folding process and its influence on the pendulum's framework structure are discussed in the following.

One of the most influential pendulum parameters, which dictates the folding process, is the kinematics of the point (P_1 , Fig. 4). It is obvious that by manipulating the kinematic excitation definition $\theta^F(t)$ and $\theta^H(t)$, different kinematic

profiles of the point P_1 are achieved and the folded layer shape on the forming conveyor manipulated (Fig. 2). The position, absolute velocity and absolute acceleration profiles of point P_1 for a specific kinematic excitation are shown in Fig. 15.

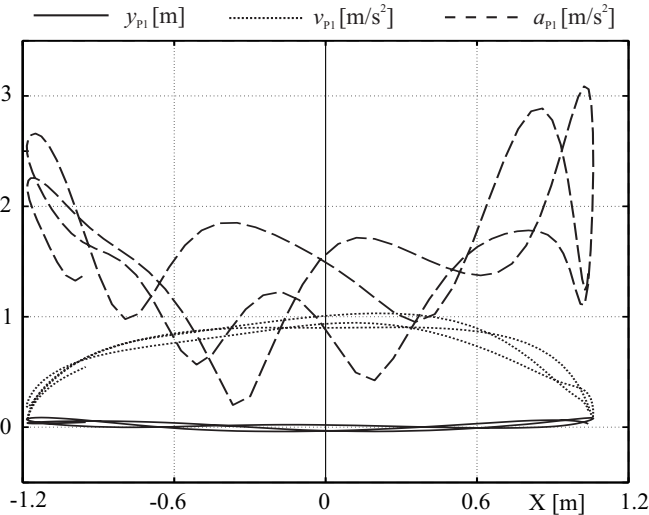


Figure 15: Position y_{P1} , absolute velocity v_{P1} and absolute acceleration a_{P1} of the point P_1

In reality, there are many pendulum excitations used and knowing the mechanism support forces for a specific excitation becomes essential. From the numerical model, these forces (Fig. 6, supp1 - supp4) can be obtained directly from the calculated forces at the points P_3 , P_4 , P_{10} and P_{11} , (Fig. 4). The support forces for the same kinematic excitation are shown in Fig. 16 and 17. The obtained support forces are applicable to the pendulum framework’s structural analysis, which is beyond the scope of this study.

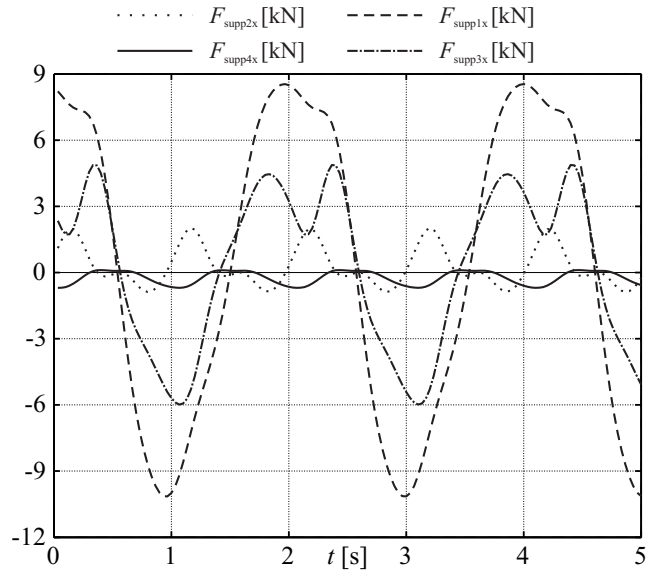


Figure 16: Pendulum support forces in horizontal direction

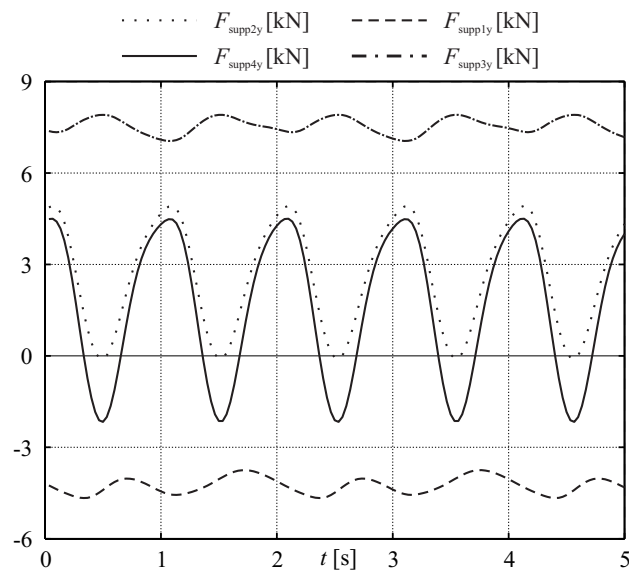


Figure 17: Pendulum support forces in vertical direction

6. Conclusion

An experimental procedure for a numerical model validation of a large-scale, rigid, multi-body system was presented. A computational dynamics approach was used to obtain the theoretical dynamical response of a planar, 24-DOF pendulum system with diverse geometry and inertia properties. The presented approach is general and is based on the formulation of the joint constraints between the system bodies. Real-time measurements were executed on the real pendulum system during its operation. Due to the concurrent measurements requirements and due to the analyzed system's relatively large dimensions, the experiments were executed with a combination of the conventional and wireless measuring equipment. The established numerical model was validated through the comparison between the several simulated and experimental kinematical and dynamical results, and good agreement was obtained between them. The planar rigid-body modelling was justified on the basis of the extensive experimental data, and the numerical model was found to have a strong predictive ability for the analyzed system's dynamical response to the arbitrary kinematic excitations.

Acknowledgments

Operation partially financed by the European Union, European Social Fund.

References

- [1] Yoo WS, Kim KN, Kim HW, Sohn JH, Developments of multibody system dynamics: computer simulations and experiments, *Multibody System Dynamics* 18 (1) (2007) 35–58.
- [2] Raftoyiannis IG, Spyrakos CC, Michaltsos GT, Behavior of suspended roofs under blast loading, *Engineering Structures* 29 (1) (2007) 88 – 100.
- [3] Zhang Y, Cai CS, Load distribution and dynamic response of multi-girder bridges with frp decks, *Engineering Structures* 29 (8) (2007) 1676 – 1689.
- [4] Zhang ZC, Lin JH, Zhang YH, Zhao Y, Howson WP, Williams FW, Non-stationary random vibration analysis for train-bridge systems subjected to horizontal earthquakes, *Engineering Structures* 32 (11) (2010) 3571 – 3582.
- [5] Lee CH, Kim CW, Kawatani M, Nishimura N, Kamizono T, Dynamic response analysis of monorail bridges under moving trains and riding comfort of trains, *Engineering Structures* 27 (14) (2005) 1999 – 2013.
- [6] Slavič J, Simonovski I, Boltežar M, Damping identification using a continuous wavelet transform: application to real data, *Journal of Sound and Vibration* 262 (2) (2003) 291 – 307.
- [7] Slavič J, Boltežar M, Non-linearity and non-smoothness in multi-body dynamics: application to woodpecker toy, *Proceedings of the institution of mechanical engineers part C - Journal of mechanical engineering science* 220 (3) (2006) 285–296.

- [8] Wojtyra M, Joint reaction forces in multibody systems with redundant constraints, *Multibody System Dynamics* 14 (1) (2005) 23–46.
- [9] Shabana AA, *Computational dynamics*, 3rd edition, Cambridge University Press, 2010.
- [10] Shabana AA, *Dynamics of Multibody Systems*, 3rd edition, Cambridge University Press, 2005.
- [11] Lot R, Da Lio M, A symbolic approach for automatic generation of the equations of motion of multibody systems, *Multibody System Dynamics* 12 (2) (2004) 147–172.
- [12] Rathod C, Shabana AA, Geometry and differentiability requirements in multibody railroad vehicle dynamic formulations, *Nonlinear Dynamics* 47 (2007) 249–261.
- [13] Orlandea NV, From newtonian dynamics to sparse tableaux formulation and multi-body dynamics, *Proceedings of the Institution of Mechanical Engineers, Part K: Journal of Multi-body Dynamics* 222 (4) (2008) 301–314.
- [14] Sinokrot T, Nakhaeinejad M, Shabana AA, A velocity transformation method for the nonlinear dynamic simulation of railroad vehicle systems, *Nonlinear Dynamics* 51 (2008) 289–307.
- [15] Čepon G, Boltežar M, Dynamics of a belt-drive system using a linear complementarity problem for the belt-pulley contact description, *Journal of Sound and Vibration* 319 (3-5) (2009) 1019 – 1035.
- [16] Whelan MJ, Gangone MV, Janoyan KD, Jha R, Real-time wireless vibration monitoring for operational modal analysis of an integral abutment highway bridge, *Engineering Structures* 31 (10) (2009) 2224 – 2235.
- [17] Hernandez-Garcia MR, Masri SF, Ghanem R, Figueiredo E, Farrar CR, An experimental investigation of change detection in uncertain chain-like systems, *Journal of Sound and Vibration* 329 (12) (2010) 2395 – 2409, structural Health Monitoring Theory Meets Practice.
- [18] Pirnat M, Savšek Z, Boltežar M, Measuring Dynamic Loads on a Foldable City Bicycle, *Strojniški vestnik- Journal of mechanical engineering* 57 (1) (2011) 21–26.
- [19] Zupančič B, Karba R, Control Engineering: New Trends with OO Modelling Approach, *Asia International Conference on Modelling and Simulation* (2007) 595–600.
- [20] Širok B, Blagojevič B, Bullen P, *Mineral wool: Production and properties*, Cambridge Intl Science Pub, 2008.